

Semiparametric Estimation of the Shape of the Limiting Multivariate Point Cloud

Reetam Majumder
SECASC
North Carolina State University
Raleigh, NC, 27695

Benjamin A. Shaby
Department of Statistics
Colorado State University
Fort Collins, CO, 80523

Brian J. Reich
Department of Statistics
North Carolina State University
Raleigh, NC, 27695

Daniel Cooley
Department of Statistics
Colorado State University
Fort Collins, CO, 80523

November 23, 2023

Abstract

We propose a model to flexibly estimate joint tail properties by exploiting the convergence of an appropriately scaled point cloud onto a compact limit set. Characteristics of the shape of the limit set correspond to key tail dependence properties. We directly model the shape of the limit set using Bézier splines, which allow flexible and parsimonious specification of shapes in two dimensions. We then fit the Bézier splines to data in pseudo-polar coordinates using Markov chain Monte Carlo, utilizing a limiting approximation to the conditional likelihood of the radii given angles. By imposing appropriate constraints on the parameters of the Bézier splines, we guarantee that each posterior sample is a valid limit set boundary, allowing direct posterior analysis of any quantity derived from the shape of the curve. Furthermore, we obtain interpretable inference on the asymptotic dependence class by using mixture priors with point masses on the corner of the unit box. Finally, we apply our model to bivariate datasets of extremes of variables related to fire risk and air pollution.

Keywords: Bayesian inference, Bézier curves, extreme values, gauge function, limit set

1 Introduction

Multivariate tail risk calculations require knowledge of the strength of dependence in the joint tail of the relevant distribution. Here, we propose a model to flexibly estimate joint tail characteristics in a way that coherently links several existing measures of tail dependence. To do this, we describe tail dependence of a multivariate distribution through its associated *gauge function* (Balkema et al., 2010; Balkema and Nolde, 2010; Nolde, 2014). The homogeneity property of the gauge function allows us to recover the entire gauge function from its unit level set, which bounds the support of the appropriately scaled data points in the limit (Nolde and Wadsworth, 2022; Wadsworth and Campbell, 2022). We represent the unit level set of the gauge function using a semiparametric model, specified such that the required constraints on such functions are automatically satisfied. In this way, we obtain a posterior sample of gauge functions, with each member of the sample being a valid gauge function not requiring any re-scaling or truncation.

Efforts to exploit the limit set representation of multivariate extreme values (Davis et al., 1988; Kinoshita and Resnick, 1991; Balkema et al., 2010; Balkema and Nolde, 2010) have appeared only recently. Wadsworth and Campbell (2022) decompose the data into pseudo-polar coordinates and use a limiting argument to approximate the distribution of the radii with a truncated Gamma distribution whose parameters depend on

the gauge function. They first transform the data to unit exponential margins, and assume a parametric form for the gauge function, and perform maximum likelihood estimation with the truncated Gamma likelihood. They extend this approach using mixtures of parametric forms, but need to perform post-hoc re-scaling of the mixtures to satisfy the required properties of valid gauge functions.

Simpson and Tawn (2022) take a more flexible nonparametric approach. They estimate the sample limit set by approximating the limiting upper endpoint of the distribution of radii with an estimated high quantile, as a function of angle. To do this, they fit a generalized Pareto distribution, whose scale parameter varies by angle, to the large radii. The radii are calculated by decomposing the bivariate data points, which have been transformed to unit exponential with a rank transformation and scaled by $\log n$. As the result is not a valid limit set, they perform a subsequent scaling and truncation procedure based on a Hill estimator to force their estimate to satisfy the required conditions.

Here, we directly model the boundary of the limiting scaled point cloud, which is prescribed by the unit level set of the gauge function, as a Bézier spline (for reviews, see Hazewinkel, 2012; Farouki, 2012). Similar semiparametric approaches have been used previously in multivariate extremes to characterize the Pickands dependence function, a different function which describes extremal dependence (Marcon et al., 2014, 2017; Vettori et al., 2018), and the angular dependence function (Murphy-Barltrop et al., 2023), which we will explore below as a direct byproduct of the gauge function. Bézier splines are convenient here because they allow parsimonious specification of shapes in \mathbb{R}^2 which are defined by a small number of control points. Placing appropriate constraints on the control points can ensure that the resultant shapes satisfy the conditions required of limit set boundaries. To estimate the parameters of the Bézier spline, we use the result from Wadsworth and Campbell (2022) which says that, given a gauge function evaluated at the data points, the distribution of the large radial components decays like a Gamma distribution whose rate parameter depends on the gauge function. We then use standard Markov chain Monte Carlo machinery to sample from the posterior distribution.

Our approach has several advantages. First, we model the shape of the limiting point cloud in a way that automatically results in a valid limit set, without the need for *ad hoc* fixes. Second, our model allows boundary of the limit set to exactly touch the corners of the unit box, giving a clean interpretation of the distinction between asymptotic independence and asymptotic dependence classes. Finally, our approach produces a posterior sample of valid limit set curves which yields a realistic picture of the state of knowledge about the joint tail region given the data.

The rest of the paper is arranged as follows. Section 2 introduces the limiting scaled point cloud and how it can be used to model the tail behavior of bivariate data. Section 3 develops the modeling of the limit set boundary using Bézier splines. Section 4 contains two simulation studies demonstrating our approach. Section 5 contains two applications—the Santa Ana Winds dataset, and ozone concentration data for the contiguous US—where we use Bézier splines to model the tail dependence in the data. Section 6 concludes.

2 The Limiting Scaled Point Cloud

Consider a collection of n independent random vectors in \mathbb{R}_+^2 , $\mathbf{X}_1, \dots, \mathbf{X}_n$, each having joint density $f_{\mathbf{X}}$, with standard exponential margins. At times, it will be convenient to transform the components of $\mathbf{X} = (X_1, X_2)^T$ into pseudo-polar coordinates (R, W) , as $R = X_1 + X_2$, and $W = X_1/R$.

Now define the scaled point cloud as the collection of points divided by $\log n$, $\{\mathbf{X}_1/\log n, \dots, \mathbf{X}_n/\log n\}$. If we assume that $\lim_{t \rightarrow \infty} -\log f_{\mathbf{X}}(t\mathbf{x})/t = g(\mathbf{x})$, $\mathbf{x} \in \mathbb{R}_+^2$, for some function g , then the scaled point cloud converges onto a compact limit set

$$G = \{\mathbf{x} \in \mathbb{R}^2 : g(\mathbf{x}) \leq 1\}$$

as $n \rightarrow \infty$ (Davis et al., 1988; Kinoshita and Resnick, 1991; Nolde, 2014; Nolde and Wadsworth, 2022). The function g is called the *gauge function* associated with the density $f_{\mathbf{X}}$. Denote the boundary of G as ∂G .

The shape of the limit set G contains useful information about the extremal dependence of the distribution of the data. Nolde and Wadsworth (2022) linked particular features of the shape of G with various indices of joint tail dependence in the literature. The residual tail dependence coefficient (Ledford and Tawn, 1996), the angular dependence function (Wadsworth and Tawn, 2013), components of the conditional extremes model (Heffernan and Tawn, 2004), and others all have direct connections to the shape of G . Our primary focus is on the residual tail dependence coefficient, $\eta \in (0, 1]$, which is defined by assuming that, for \mathbf{X} in

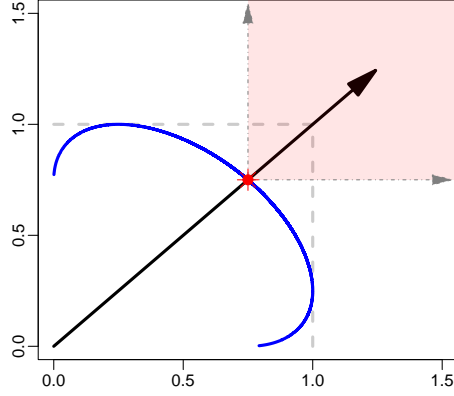


Figure 1: Schematic of η . The blue curve is the unit level set of gauge function $g(\mathbf{x})$, which forms the limit set boundary ∂G , and the proportional distance to the red point from the origin is the tail dependence coefficient η .

exponential margins, its survivor function satisfies

$$P(X_1 > x, X_2 > x) = \mathcal{L}(e^x)e^{-x/\eta}$$

for some function \mathcal{L} that is slowly varying at infinity (Ledford and Tawn, 1996). Then the coefficient η describes the strength of dependence in the joint tail, with $\eta \in (1/2, 1)$ indicating positive tail dependence but independence in the limit $x \rightarrow \infty$ (i.e asymptotic independence) and $\eta = 1$ indicating asymptotic dependence, i.e.,

$$\lim_{x \rightarrow \infty} \frac{P(X_1 > x, X_2 > x)}{P(X_1 > x)} > 0,$$

assuming $\mathcal{L}(x) \rightarrow 0$.

The residual tail dependence coefficient, η , can be calculated (Nolde and Wadsworth, 2022) from shape of the limit set as

$$\eta = \min\{r : r \times [1, \infty]^2 \cap G = \emptyset\}.$$

This is illustrated schematically in Figure 1, where one can think of sliding the shaded box down the ray with slope 1 until it first touches the boundary ∂G . The radius corresponding to this first point of intersection is η . A corollary is that (barring exotic edge cases) when \mathbf{X} is asymptotically dependent, $\eta = 1$, so ∂G necessarily touches the upper right-hand corner of the unit box. Conversely, when \mathbf{X} is asymptotically independent, $\eta < 1$, so ∂G does not touch the upper right-hand corner, and is referred to as *blunt*.

Every gauge function g is homogeneous of order one, with $g(c\mathbf{x}) = cg(\mathbf{x})$ for any $c > 0$ (Nolde, 2014). We will use this property by modeling the limit set boundary ∂G directly and using its associated gauge function, induced by homogeneity, for estimation (see Section 3.1). Any valid limit set G must satisfy the following constraints on its shape:

1. G is *star-shaped*, meaning that for any $t \in (0, 1)$, if \mathbf{x} is in G , then $t\mathbf{x}$ is also in G .
2. The supremum of the boundary ∂G is 1 in each component direction. That is, ∂G touches, but does not cross, the upper and right-hand sides of the unit box.

We seek a flexible way of representing the boundary ∂G of the limit set G that satisfies conditions 1 and 2 and can be estimated from *iid* samples of the random vector \mathbf{X} .

3 Modeling the Shape Using Bézier Splines

Bézier curves (e.g. Hazewinkel, 2012; Farouki, 2012) are a class of parametric functions that can be used as building blocks to represent complex shapes. Bézier curves are defined by a set of *control points* \mathbf{p}_0 to \mathbf{p}_m ,

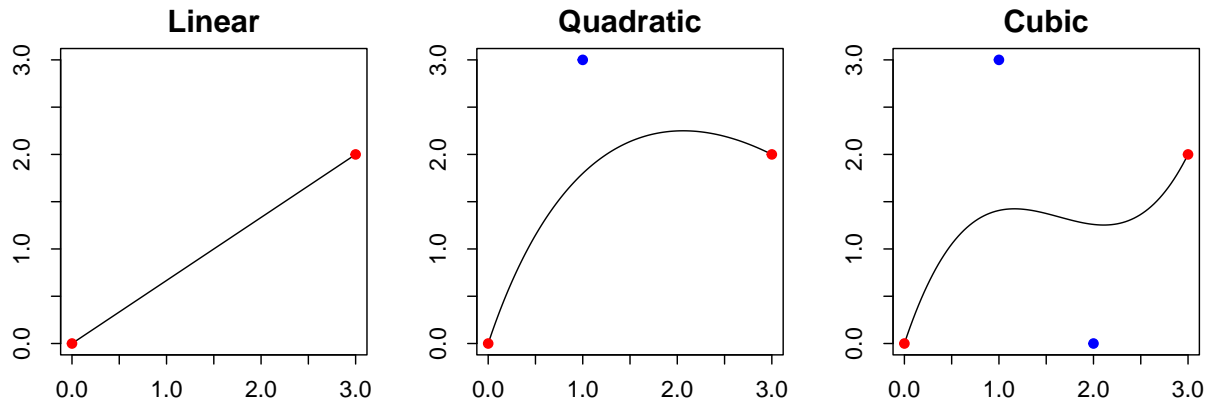


Figure 2: Examples of Bézier curves of orders 1, 2, and 3. The red control points (end points) \mathbf{p}_0 and \mathbf{p}_m always lie on the curve, while the blue control points usually do not.

where m is the order of the curve. Figure 2 plots examples of Bézier curves of orders 1–3. The end points (red) define the beginning and end of the curve; intermediate control points (blue) of each curve control its shape but generally do not lie on the curve. A quadratic Bézier curve, for example, traces the path:

$$B(t) = (1-t)[(1-t)\mathbf{p}_0 + t\mathbf{p}_1] + t[(1-t)\mathbf{p}_1 + t\mathbf{p}_2],$$

for $0 \leq t \leq 1$. Rearranging this equation simplifies it to:

$$B(t) = (1-t)^2\mathbf{p}_0 + 2t(1-t)\mathbf{p}_1 + t^2\mathbf{p}_2.$$

A useful property is that if the three points are co-linear, then a quadratic Bézier curve simplifies to a linear Bézier curve. Several Bézier curves can in turn be linked together at the end points to form a Bézier spline. The end points of the each Bézier curve within the spline now function as *knots* for the spline. Splines comprised of quadratic Bézier curves are particularly useful since analytical solutions for quadratic equations are straightforward to obtain. In addition, increasing the order to cubic splines would make it difficult to constrain the shapes to the unit box, and would prevent the shapes from having the sharp corners required to represent asymptotically dependent limit set boundaries.

Because they are parsimoniously parameterized and straightforward to constrain, Bézier splines are convenient for modeling the boundary ∂G of the limit set G . We specify ∂G as a Bézier spline comprised of three quadratic Bézier curves $g_B = \{B_1(t), B_2(t), B_3(t)\}$, where $B_1(t) := B(t; \mathbf{p}_0, \mathbf{p}_1, \mathbf{p}_2)$, $B_2(t) := B(t; \mathbf{p}_2, \mathbf{p}_3, \mathbf{p}_4)$, and $B_3(t) := B(t; \mathbf{p}_4, \mathbf{p}_5, \mathbf{p}_6)$, for $\mathbf{p}_i \in \mathbb{R}^2$, $i = 0, 1, \dots, 6$. The three curves trace the paths:

$$\begin{aligned} B_1(t) &= (1-t)^2\mathbf{p}_0 + 2t(1-t)\mathbf{p}_1 + t^2\mathbf{p}_2, \\ B_2(t) &= (1-t)^2\mathbf{p}_2 + 2t(1-t)\mathbf{p}_3 + t^2\mathbf{p}_4, \\ B_3(t) &= (1-t)^2\mathbf{p}_4 + 2t(1-t)\mathbf{p}_5 + t^2\mathbf{p}_6, \end{aligned}$$

for $0 \leq t \leq 1$. We denote the point $\mathbf{p}_i := (p_{i,1}, p_{i,2})$, $0 \leq p_{i,1}, p_{i,2} \leq 1$, and place two sets of constraints on the curves in order to elicit valid gauge functions which satisfy conditions 1 and 2. The first set of constraints ensure that the Bézier spline touches all four edges of the unit square:

$$\begin{aligned} p_{0,1} &= p_{6,2} = 0, \\ p_{2,2} &= p_{4,1} = 1. \end{aligned}$$

The second set of constraints are sufficient conditions to ensure that the star-shaped property holds for the

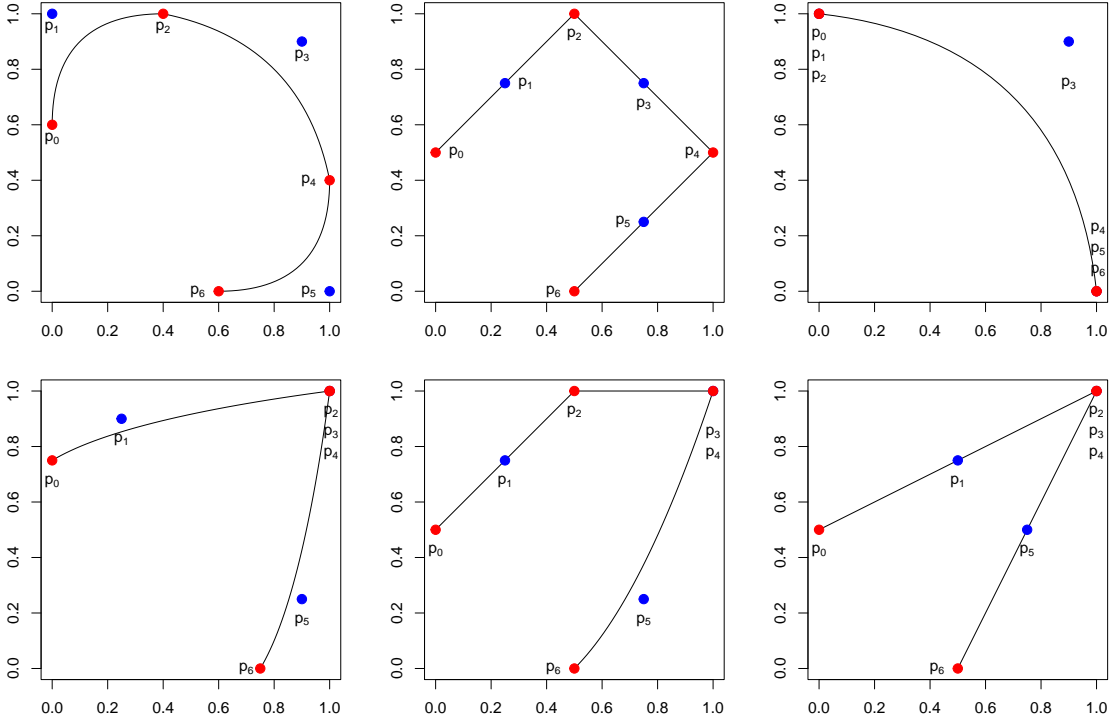


Figure 3: Examples of unit level sets of gauge functions that can be expressed using Bézier splines comprised of 3 quadratic Bézier curves. The red points are the end points of each curve, while the blue points are intermediate points controlling the shapes of the curves.

spline:

$$\begin{aligned}
 p_{1,2} &\geq p_{0,2}, \\
 m(\mathbf{p}_0, \mathbf{p}_1) &\geq m(\mathbf{p}_0, \mathbf{p}_2), \\
 p_{3,1} &= p_{3,2}, \\
 m(\mathbf{p}_4, \mathbf{p}_6) &\geq m(\mathbf{p}_5, \mathbf{p}_6), \\
 p_{6,1} &\leq p_{5,1},
 \end{aligned}$$

where $m(\mathbf{p}, \mathbf{p}')$ denotes the slope of the line connecting the points \mathbf{p} and \mathbf{p}' . Thus, we arrive at a model for the limit set boundary ∂G , indexed by the 9 univariate parameters $\boldsymbol{\theta}_g = (p_{0,2}, p_{1,1}, p_{1,2}, p_{2,1}, p_{3,1}, p_{4,2}, p_{5,1}, p_{5,2}, p_{6,1})^T$.

Figure 3 plots Bézier splines under these constraints, each representing a gauge function with different dependence properties. Top row plots correspond to asymptotic independence scenarios, whereas plots in the bottom row correspond to asymptotic dependence scenarios. The four red control points are the knots of the spline. The three blue control points affect the shape, and the spline passes through them only if they are co-linear with the preceding and proceeding control points. In the general case, there are 9 coordinates, each admitting a uniform support, which need to be estimated to fully specify a valid gauge function. Richer models can be achieved using more control points; however, it would come with increased computational cost and additional constraints to ensure that Conditions 1 and 2 hold. The quadratic Bézier spline with 4 knots therefore constitutes a parsimonious representation for ∂G which is still flexible enough to capture multiple dependence regimes and mimic most of the common parametric models.

3.1 Statistical inference for the limit set boundary

With a model defined for the limit set boundary ∂G , we turn to the question of how to estimate the shape from *iid* copies of the random vector \mathbf{X} in standard exponential margins. After transforming \mathbf{X} to pseudo-

polar coordinates (R, W) , a convenient form (Wadsworth and Campbell, 2022) for the conditional density of a large radius R , given the angle W , is

$$f_{R|W}(r|w) \propto r^{d-1} \exp\{-rg(r, w)[1 + o(1)]\}, \quad r \rightarrow \infty,$$

where d is the dimension of \mathbf{X} (we have only considered $d = 2$ here). For likelihood-based inference, Wadsworth and Campbell (2022) ignore the $o(1)$ term and consider the approximation adequate for radii larger than a threshold $r_0(w)$, which yields a truncated Gamma likelihood:

$$R|W = w, R > r_0(w), \boldsymbol{\theta}_g \sim \text{truncGamma}(\alpha, g_{\boldsymbol{\theta}_g}(r, w)), \quad (1)$$

where the limiting value of α is $d = 2$. Thus, given a gauge function $g_{\boldsymbol{\theta}_g}$, an approximate likelihood for the large radii, given the angles, is

$$L(\boldsymbol{\theta}_g, \alpha; (r_1, w_1), \dots, (r_{n_0}, w_{n_0})) = \prod_{i=1}^{n_0} \frac{g_{\boldsymbol{\theta}_g}(r, w)^\alpha}{\Gamma(\alpha)} \frac{r_i^{\alpha-1} e^{-r_i g_{\boldsymbol{\theta}_g}(r_i, w_i)}}{1 - F(r_0(w_i); \alpha, g_{\boldsymbol{\theta}_g}(r_i, w_i))}, \quad (2)$$

where n_0 is the number of points exceeding the threshold $r_0(w)$, and $F(\cdot; \alpha, g_{\boldsymbol{\theta}_g}(r_i, w_i))$ is the CDF of a Gamma distribution with shape parameter α and rate parameter $g_{\boldsymbol{\theta}_g}(r_i, w_i)$.

An alternative to using only the large radii with a truncated Gamma likelihood is to consider all of the data points and censor the radii that are below the threshold $r_0(w)$. This yields the slightly different, censored Gamma likelihood

$$L_C(\boldsymbol{\theta}_g, \alpha; (r_1, w_1), \dots, (r_n, w_n)) = \prod_{i=1}^n L_i(\boldsymbol{\theta}_g, \alpha; (r_i, w_i),$$

with

$$L_i(\boldsymbol{\theta}_g, \alpha; (r_i, w_i)) = \begin{cases} F(r_0(w_i); \alpha, g_{\boldsymbol{\theta}_g}(r_0, w_i)), & r_i < r_0(w_i), \\ f(r_i(w_i); \alpha, g_{\boldsymbol{\theta}_g}(r_i, w_i)), & r_i \geq r_0(w_i), \end{cases} \quad (3)$$

where $f(\cdot; \alpha, g_{\boldsymbol{\theta}_g}(r_i, w_i))$ is the density of a Gamma distribution with shape parameter α and rate parameter $g_{\boldsymbol{\theta}_g}(r_i, w_i)$.

There are potential advantages of using the censored likelihood (3) on *all* of the data rather than the truncated likelihood (2) on just the data with large radii. Intuitively, if the likelihood “knows” which angles correspond to small radii, that additional information could help it estimate the shape of limit set boundary ∂G more accurately, while censoring the small radii should mitigate any biasing effect. In contrast, the truncated likelihood is not given information about which angles correspond to small radii. We explore this issue in Section 4.2 using a simulation study.

To calculate the gauge function at each data point, as required in the likelihoods (2) and (3), we exploit the homogeneity property of g . This gives us that the value of the gauge function evaluated at a point \mathbf{x} is the distance from the origin to \mathbf{x} , relative to the distance from the origin of the intersection of the ray connecting \mathbf{x} with the origin and the boundary ∂G . In the schematic in Figure 4, the intersection with ∂G is denoted as $\mathbf{x}_{\partial G}$, so that

$$g_{\boldsymbol{\theta}_G}(\mathbf{x}) = \frac{\|\mathbf{x}\|}{\|\mathbf{x}_{\partial G}\|}. \quad (4)$$

We also need to select a threshold $r_0(w)$, as a function of angle. Wadsworth and Campbell (2022) and Simpson and Tawn (2022) both choose complicated thresholds, first as empirical quantiles in moving windows of angles, and then using smooth semiparametric quantile regression. Instead, we simply choose a high quantile in each marginal component. We have found that this very basic strategy results in estimation performance at least comparably as good as more complicated alternatives. In addition, choosing marginal thresholds has two key advantages. First, it is simple to implement and requires no intricate tuning. Second, it permits, in principle, transformation to standard exponential margins within a hierarchical model, whereas thresholds that depend jointly on both components do not. With this in mind, we choose a value $\tau \in (0, 1)$, and then set each marginal threshold at the τ^{th} marginal empirical quantile. A sensitivity study comparing the effect of the choice of threshold on estimation of η is provided in the Supplementary Material (Majumder et al., 2023).

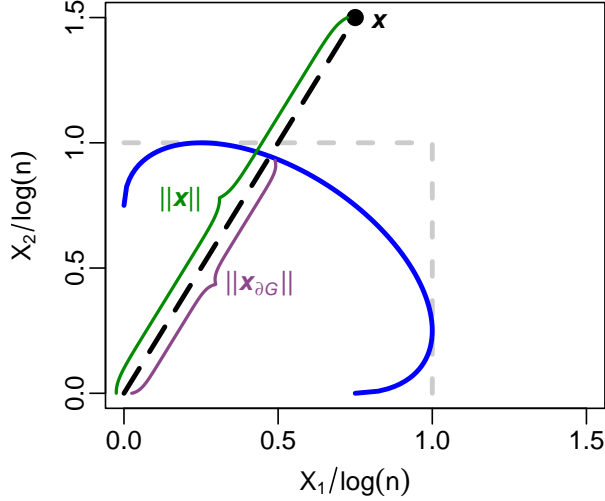


Figure 4: Schematic of how to calculate g_{θ_G} at a data point (\mathbf{x}) , given a boundary curve ∂G . The value of the gauge function is the distance from the origin to \mathbf{x} , relative to the distance from the origin of the intersection of the ray connecting \mathbf{x} with the origin and the boundary ∂G .

3.2 Limit set boundaries and prior distributions for control points

Our model for the limit set boundary ∂G is indexed by the 9 univariate parameters $\theta_g = (p_{0,2}, p_{1,1}, p_{1,2}, p_{2,1}, p_{3,1}, p_{4,2}, p_{5,1}, p_{5,2}, \alpha)$. To inform prior selection for these control points, we examine the boundary ∂G of three parametric copula models, and learn the conditions on the control points which allow the Bézier curve to mimic their shapes. The three copulas that we consider are the Gaussian, inverted logistic, and logistic. The first two are asymptotically independent, while the last one is asymptotically dependent; analytical expressions of dependence measures for these models are provided in Table 1, replicated from Simpson and Tawn (2022). Since the limit set boundary ∂G can take on a variety of shapes, including the asymptotic dependence case where it touches the upper right-hand corner of the unit box (see e.g., Nolde and Wadsworth, 2022, Section 4), we let the control points vary freely in $(0, 1)$ for flexibility, and permitting the possibility of being exactly equal to 0 or 1 to accommodate both asymptotic dependence as seen in the logistic copula and the very weak dependence as seen in the inverted logistic copula. We now outline the support for the distributions of the control points which will allow the Bézier splines to mimic our three copulas of interest, and then specify priors for all parameters to be used in the remainder of this study.

The limit set boundary for a logistic dependence copula is obtained when $\mathbf{p}_2 = \mathbf{p}_3 = \mathbf{p}_4 = (1, 1)$ (Figure 3, bottom-right). This is equivalent to collapsing the second curve of the Bézier spline to a single point, and can be incorporated into our model by having a semi-continuous prior distribution for $p_{2,1}, p_{3,1}$, and $p_{4,2}$ with support over $(0, 1]$ which includes a point mass at 1. Similarly, approximating the limit set boundary for an inverted logistic copula using a Bézier spline would require the first and third curves to collapse onto the $x = 0$ and $y = 0$ lines respectively (Figure 3, top-right). To accommodate this case, we set semi-continuous priors with point masses at 0 for $p_{1,1}, p_{2,1}, p_{4,2}$, and $p_{5,2}$, and point masses at 1 for $p_{1,2}$ and $p_{5,1}$. This allows us to have an exact representation of the logistic and a very close approximation for the inverted logistic copula. For priors, we set:

$$\begin{aligned} \alpha &\sim \text{LogNormal}(1, 1), \\ \Phi^{-1}(p_{0,2}), \Phi^{-1}(p_{6,1}) &\sim \text{Normal}(0, 0.5^2), \\ p_{1,2}, p_{5,1} &\sim \text{Uniform}(0, 1). \end{aligned}$$

The LogNormal prior on α has its density concentrated near $\alpha = 2$. The control points $p_{0,2}$ and $p_{6,1}$ are the knots at the two ends of the Bézier spline, and is rarely too close to either boundary (0 or 1) in most practical

Measure	Gaussian	Logistic	Inverted logistic
$g(\mathbf{x}) = g(x_1, x_2)$	$\frac{x_1+x_2-2\rho(x_1x_2)^{1/2}}{1-\rho^2}$	$\frac{1}{\theta} \max(x_1, x_2) + (1 - \frac{1}{\theta}) \min(x_1, x_2)$	$(x_1^{1/\theta} + x_2^{1/\theta})^\theta$
η	$\frac{1+\rho}{2}$	1	$2^{-\theta}$
$\lambda(\omega, 1 - \omega)$	$\begin{cases} \max(\omega, 1 - \omega), & \text{if } t_\omega \leq \rho^2 \\ \frac{1-2\rho\sqrt{\omega(1-\omega)}}{1-\rho^2}, & \text{if } t_\omega \geq \rho^2 \end{cases}$	$\max(\omega, 1 - \omega)$	$g(\omega, 1 - \omega)$
$\tau_1(\delta) = \tau_2(\delta)$	$\begin{cases} 1, & \text{if } \delta \geq \rho^2 \\ \frac{1-\rho^2}{1+\delta-2\rho\sqrt{\delta}}, & \text{if } \delta \leq \rho^2 \end{cases}$	$[\theta^{-1} + (1 - \theta^{-1}\delta)]^{-1}$	1

Table 1: Gauge function g , and a summary of dependence measures for the three bivariate copulas used in our study. Here, $t_\omega = \min(\omega, 1 - \omega) / \max(\omega, 1 - \omega)$. Table has been reproduced from [Simpson and Tawn \(2022\)](#).

cases. Its prior density is therefore concentrated around 0.5. The remaining control points have priors that are the mixture of a standard Uniform distribution and at least one point mass (to allow important geometric features of ∂G with positive probability). They have the following forms:

$$\begin{aligned} p_{1,1} &\sim 0.1 \cdot \mathbb{I}(p_{1,1} = 0) + 0.9 \cdot \text{Uniform}(0, 1), \\ p_{2,1} &\sim 0.1 \cdot \mathbb{I}(p_{2,1} = 0) + 0.6 \cdot \text{Uniform}(0, 1) + 0.3 \cdot \mathbb{I}(p_{2,1} = 1), \\ p_{3,1} &\sim 0.7 \cdot \text{Uniform}(0, 1) + 0.3 \cdot \mathbb{I}(p_{3,1} = 1). \end{aligned}$$

The control point $p_{5,2}$ has the same mixture prior as $p_{1,1}$, while $p_{4,2}$ has the same mixture prior as $p_{2,1}$. The point mass probabilities were chosen on the basis of a sensitivity study whose aim was to have good discrimination between asymptotic dependence and independence cases based on posterior probabilities of $\eta = 1$, while also simultaneously being able to provide unbiased, consistent estimates of η when $\eta < 1$. Our choices of the mixture probabilities prescribe that the prior probability of a point mass at (1,1) (corresponding to asymptotic dependence as in the logistic copula) is 0.025, and the prior probability a point mass at (0,1) or (1,0) (corresponding to a shape like that of an inverted logistic copula) are each 0.01. These prior assumptions can accommodate the logistic copula and inverted logistic copulas, as well as intermediate forms such as the Gaussian copula which do not require point masses.

3.3 Additional bivariate extremal dependence measures

Alongside the tail dependence coefficient η ([Ledford and Tawn, 1996](#)) discussed in Section 2, we consider two related indices of tail dependence which can be derived from the gauge function. The first of these is the angular dependence function $\lambda(\omega)$ which considers different scalings for the two components of \mathbf{X} . In particular, [Wadsworth and Tawn \(2013\)](#) considered limiting probabilities of the following form:

$$P(X_1 > \omega x, X_2 > (1 - \omega)x) = \mathcal{L}_\omega(e^x) e^{-x\lambda(\omega)},$$

for $\omega \in (0, 1)$, $\lambda(\omega) \in (0, 1]$, and some function \mathcal{L}_ω that is slowly varying at infinity. Thus, $\lambda(\omega)$ is a generalization of η , with $\eta = 1/\{2\lambda(1/2)\}$. We also investigate the dependence measure $\tau_1(\delta)$ ([Simpson et al., 2020](#)), given by:

$$P(X_1 > x, X_2 \leq \delta x) = \mathcal{L}_\delta(e^x) e^{-x/\tau_1(\delta)},$$

for some function \mathcal{L}_δ that is slowly varying at infinity, with $\delta \in (0, 1)$. This dependence measure specifically characterizes the probability of X_1 being large while X_2 is of a smaller order. We can define $\tau_2(\delta)$ analogously, and both $\tau_1(\delta), \tau_2(\delta) \in (0, 1]$.

Table 1 provides the analytical expressions for these measures for the three dependence copulas that we consider in our study. Like with η , these dependence measures can be exactly deduced from the gauge functions. Since the Bézier splines are quadratic polynomials, we can easily calculate $\tau_1(\delta)$ and $\lambda(\omega)$ for any estimated limit set boundary, simply by finding the intersections of polynomials and lines, which have closed-form solutions. Note that while we do not present results for $\tau_2(\delta)$ in our study, it can be calculated in the same manner as $\tau_1(\delta)$. We refer the reader to [Simpson and Tawn \(2022\)](#) for a detailed discussion on how each of these measures can be obtained from gauge functions in more general settings.

4 Simulation Study

We demonstrate the appropriateness of using Bézier splines to model the limit set boundary corresponding to the gauge function by means of two simulation studies. We consider three bivariate copulas to generate dependent data with exponential marginal distributions: the Gaussian, the logistic, and the inverted logistic. The Gaussian copula is parameterized by its correlation $\rho \in [0, 1)$, while the dependence parameter for the logistic and inverted logistic copulas is $\theta \in (0, 1)$. Table 1 lists the gauge functions associated with each copula, as well as the set of corresponding extremal dependence coefficients $\{\eta, \lambda(\omega), \tau_1(\delta)\}$. The three copulas cover a range of asymptotic dependence behavior; the logistic copula, in particular, is asymptotically dependent. Further details for these three copulas can be found in [Nolde and Wadsworth \(2022\)](#). For each copula, we consider two parameter settings: $\rho = \{0.6, 0.8\}$ for the Gaussian copula, $\theta = \{0.6, 0.8\}$ for the logistic copula, and $\theta = \{0.3, 0.6\}$ for the inverted logistic copula. Smaller values of θ give stronger tail dependence for the logistic and inverted logistic copulas, whereas larger values of ρ lead to stronger tail dependence in the Gaussian copula. The data in both studies are analyzed in pseudo-polar coordinates (R, W) .

In the first study, we simulate 5,000 data points, and data that lie above at least one marginal threshold corresponding to $\tau = 0.80$ are approximated as a truncated Gamma distribution with a common shape parameter α and a rate parameter equal to an appropriate gauge function evaluated at the data point. We compare our estimated limit set boundaries with those obtained from [Simpson and Tawn \(2022\)](#) in terms of how well they estimate the set of dependence coefficients outlined in Table 1. The Simpson-Tawn estimator was also obtained using a quantile level of $\tau = 0.80$. We use the root mean square error (RMSE) to compare estimates of the scalar η , and the root mean integrated square error (RMISE) to compare estimates of the functions $\lambda(\omega)$ and $\tau_1(\delta)$. Additionally, we compare our estimates of η against the corresponding Hill-type maximum likelihood estimate ([Hill, 1975](#); [Ledford and Tawn, 1996](#)) as provided in [Simpson and Tawn \(2022\)](#).

In the second study, we explore the effect of using a censored Gamma distribution instead of a truncated Gamma distribution for points above at least one marginal threshold. Unlike the truncated Gamma likelihood where the gauge functions are estimated based on only the points that are above the quantile threshold, the censored Gamma likelihood estimates the gauge functions based on all data, with the likelihood censored below our chosen threshold. This is pertinent in cases where there are relatively few points above the marginal threshold either due to the overall size of the dataset or the threshold of choice; often both. We consider $\tau = 0.95$ for the censored Gamma likelihood model and $\tau = 0.80$ for the truncated Gamma likelihood model, and compare estimates of their dependence coefficients as in the previous study. The study uses 600 data points, which corresponds to the size of the dataset used in our second application in Section 5.2.

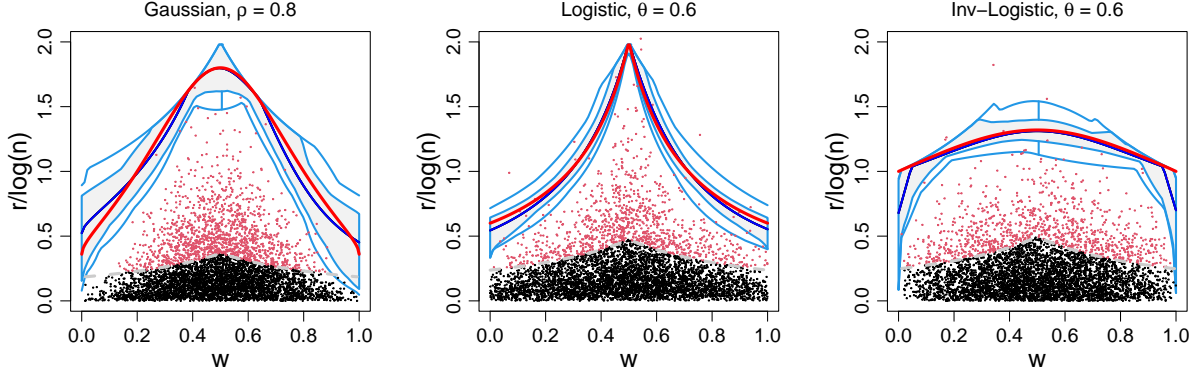
4.1 Comparison with the Simpson-Tawn estimator

4.1.1 Study Setup

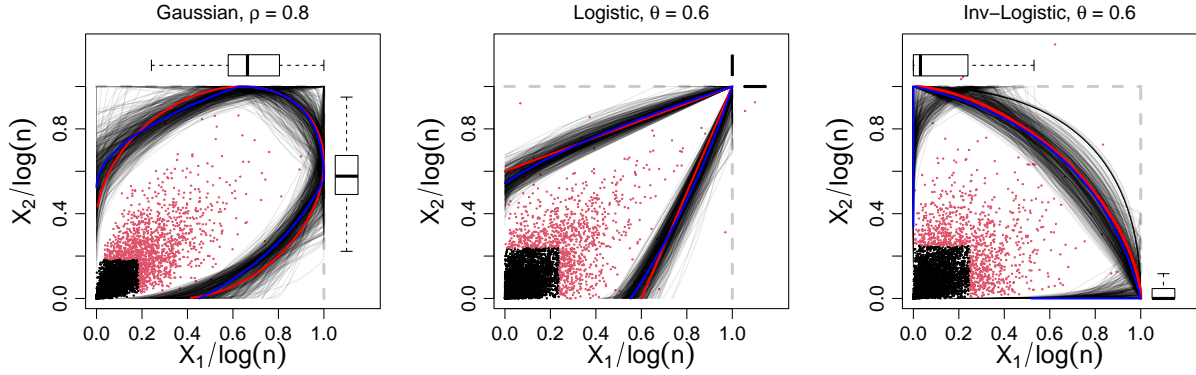
For each copula and parameter combination, we generate 100 datasets of $n = 5,000$ data points each. The datasets are converted to pseudo-polar coordinates, and the n_0 points that are above the $\tau = 0.80$ quantile marginal threshold for at least one variable are used to model the gauge function for each dataset. We use Metropolis updates for all parameters and run 11,000 MCMC iterations for each dataset, discarding the first 1,000 as burn-in. All Metropolis updates are tuned to give an acceptance probability of 0.4, and posterior convergence is diagnosed based on the visual inspection of trace plots.

4.1.2 Parameter estimates

Figure 5 plots the limit set boundaries elicited by the estimated Bézier splines based on the posterior distribution of a single dataset from each study. Plots in the upper row denote the dependence modeling in pseudo-polar coordinates. Each estimated limit set boundary is represented as a functional boxplot ([Hyndman and Shang, 2010](#); [Sun and Genton, 2011](#)), a visual representation of functional data analogous to a classical boxplot. Each functional quantile depicted in the functional boxplot is a function contained in the sample; in this case, the sample consists of limit set boundaries based on Bézier splines, in pseudo-polar coordinates, drawn from the posterior. The curves are ordered based on a notion of modified band depth ([López-Pintado and Romo, 2009](#)). The median is shown in dark blue, and the limit set boundary



(a) Estimated gauge functions in pseudo-polar space.



(b) Estimated gauge functions in Euclidean space.

Figure 5: Limit set boundaries based on Bézier splines (blue) and corresponding functions for the data-generating model (red) in pseudo-polar space (top) and Euclidean space (bottom) for Gaussian, logistic, and inverted logistic dependence copulas.

corresponding to the data-generating model is shown in red. The envelope represents the 50% central region, analogous to the box of a classical boxplot. The outer light blue lines of the functional boxplot correspond to the whiskers of a classical boxplot. Finally, the vertical lines indicate the maximum envelope of the functions except outliers. Plots in the bottom row display the dependence models in Euclidean coordinates, with the median Bézier spline in dark blue and the limit set boundary corresponding to the data-generating model in red. They are overlaid on Bézier splines evaluated from 500 random draws from the posterior distribution, plotted in gray. The boxplots on the top and right margins correspond to the posterior distributions of $p_{2,1}$ and $p_{4,2}$ respectively, which are associated with coefficients in the conditional extremes model of [Heffernan and Tawn \(2004\)](#). The Bézier splines are able to accurately represent the geometric form of all three dependence copulas. We did note that removing some of the point masses (equivalent to making prior assumptions that rule out certain copulas) led to better MCMC convergence.

Figure 6 shows boxplots of posterior median of η based on the Bézier spline estimator for the three dependence copulas in white, alongside green and blue plots that correspond to the Simpson-Tawn and Hill-type estimators respectively. The Simpson-Tawn estimators are also evaluated after setting $\tau = 0.80$. Analytical values of η obtained using expressions in [Table 1](#) are shown as red lines on each plot, and the coverage of equi-tailed 95% intervals are noted in plain text below each boxplot. Coverage for the Simpson-Tawn and Hill-type estimators are based on 100 bootstrapped samples from each of the 100 datasets. We plot the median instead of the mean for the Bézier spline estimates since the posterior distributions are often highly asymmetric due to point-mass prior distributions. The Bézier spline estimator has low bias and nominal coverage for estimates of η . The Simpson-Tawn estimator has nominal or near-nominal coverage in

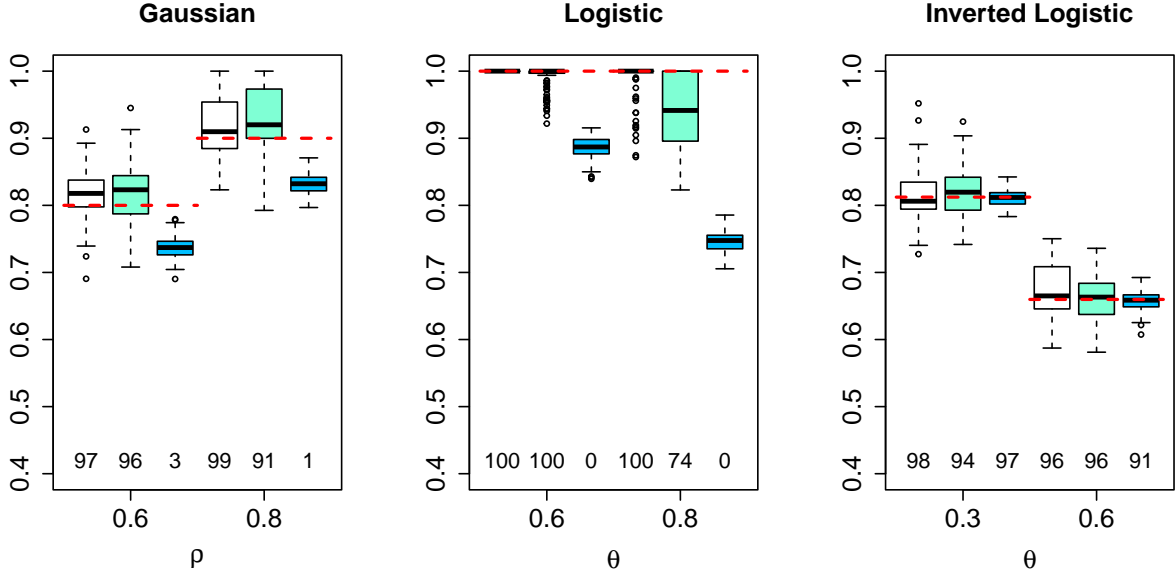


Figure 6: Sampling distribution of the posterior medians of η based on the Bézier spline estimate (white) for the three dependence copulas, alongside estimates using the Simpson-Tawn estimator (green) and the Hill-type estimator (blue). The red lines indicate the true values, and coverage of equi-tailed 95% intervals are noted below each boxplot.

Table 2: RMSE ratios for estimates of η and RMISE ratios for estimates of $\lambda(\omega)$ and $\tau_1(\delta)$ based on the Bézier spline ($\hat{\eta}$, $\hat{\lambda}$, and $\hat{\tau}$) and Simpson-Tawn ($\tilde{\eta}$, $\tilde{\lambda}$, and $\tilde{\tau}$) estimators over simulated datasets for the three copulas.

	Gaussian		Logistic		Inverted logistic	
	$\rho = 0.6$	$\rho = 0.8$	$\theta = 0.6$	$\theta = 0.8$	$\theta = 0.3$	$\theta = 0.6$
$\frac{RMSE(\tilde{\eta})}{RMSE(\hat{\eta})}$	1.24	1.02	Inf	2.69	1.03	0.72
$\frac{RMISE(\tilde{\lambda})}{RMISE(\hat{\lambda})}$	1.35	1.17	Inf	7.28	1.10	0.89
$\frac{RMISE(\tilde{\tau}_1)}{RMISE(\hat{\tau}_1)}$	1.02	1.42	1.11	1.30	0.18	0.12

most cases except for the logistic copula with very weak dependence ($\theta = 0.8$), and its bias is slightly higher than the Bézier spline estimator in all cases. The Hill-type estimator is usable only for the inverted logistic copula, and is unable to estimate η well for the other two copulas.

We evaluate $\lambda(\omega)$ and $\tau_1(\delta)$ based on the Bézier spline and Simpson-Tawn estimators for $\omega, \delta = 0.01, 0.02, \dots, 0.99$. Figure 7 shows boxplots for the posterior medians of $\lambda(0.40)$ and $\lambda(0.90)$ based on the Bézier spline estimator in white, alongside estimates based on the Simpson-Tawn estimator in green. Figure 8 similarly plots the distribution of $\tau_1(0.25)$ and $\tau_1(0.75)$ for the two estimators. Both estimators are better at estimating $\lambda(\omega)$ than $\tau_1(\delta)$, and the Bézier spline estimator tends to have better coverage than the Simpson-Tawn estimator.

Table 2 summarizes the RMSE ratio for estimates of η and RMISE ratios for estimates of $\lambda(\omega)$ and $\tau_1(\delta)$ based on the Bézier spline and Simpson-Tawn estimators. Most of the values are greater than 1, indicating that dependence measures based on Bézier spline estimates of the gauge function have comparable or better RMSE/RMISE than those based on the Simpson-Tawn estimator. In particular, the Bézier spline estimator is able to estimate $\lambda(\omega)$ exactly for $\omega = 0.01, \dots, 0.99$ for the logistic copula, leading to an RMISE of 0 and an RMISE ratio of infinity (Inf). However, for the inverted logistic copula, the Simpson-Tawn estimator

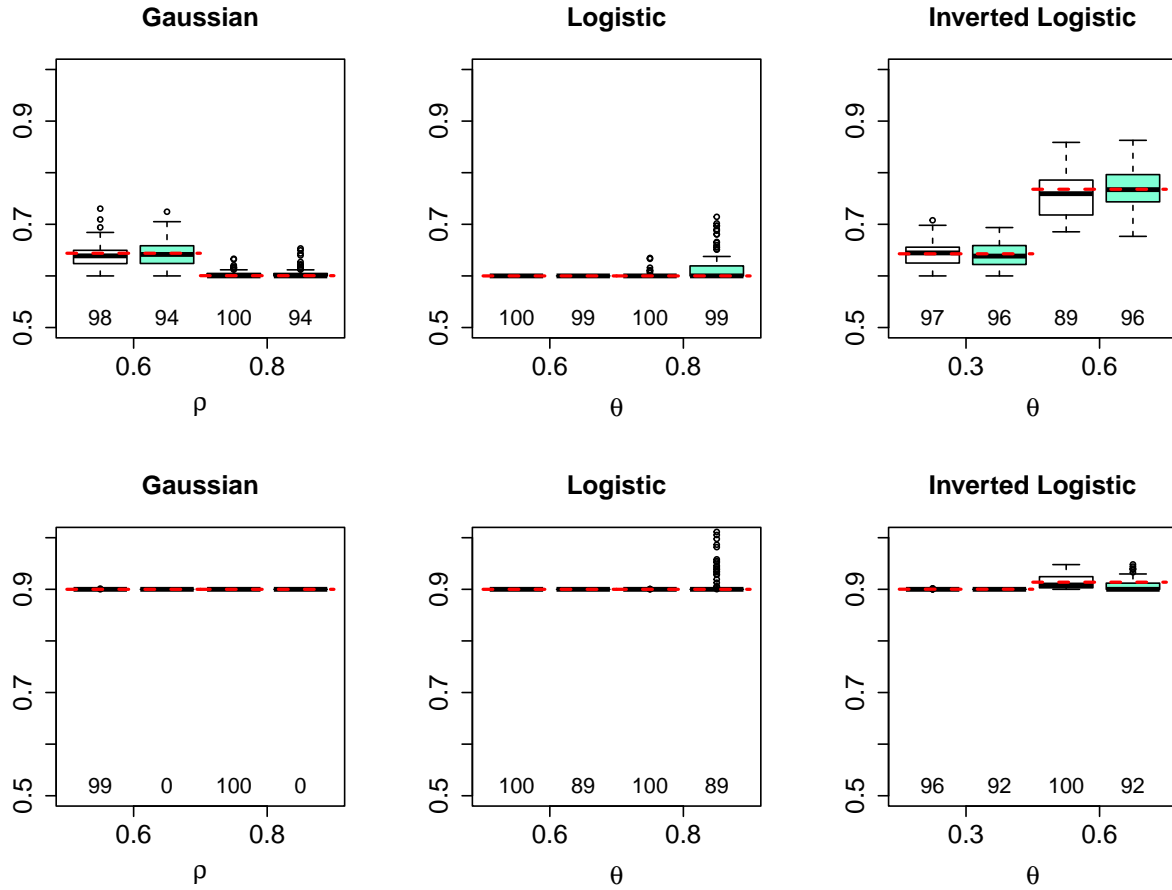


Figure 7: Sampling distribution of the posterior medians of $\lambda(0.40)$ (top) and $\lambda(0.90)$ (bottom) based on the Bézier spline estimator (white) for the three dependence copulas alongside corresponding estimates using the Simpson-Tawn estimator (green). The red lines indicate the true values, and coverage of equi-tailed 95% intervals are noted below each boxplot.

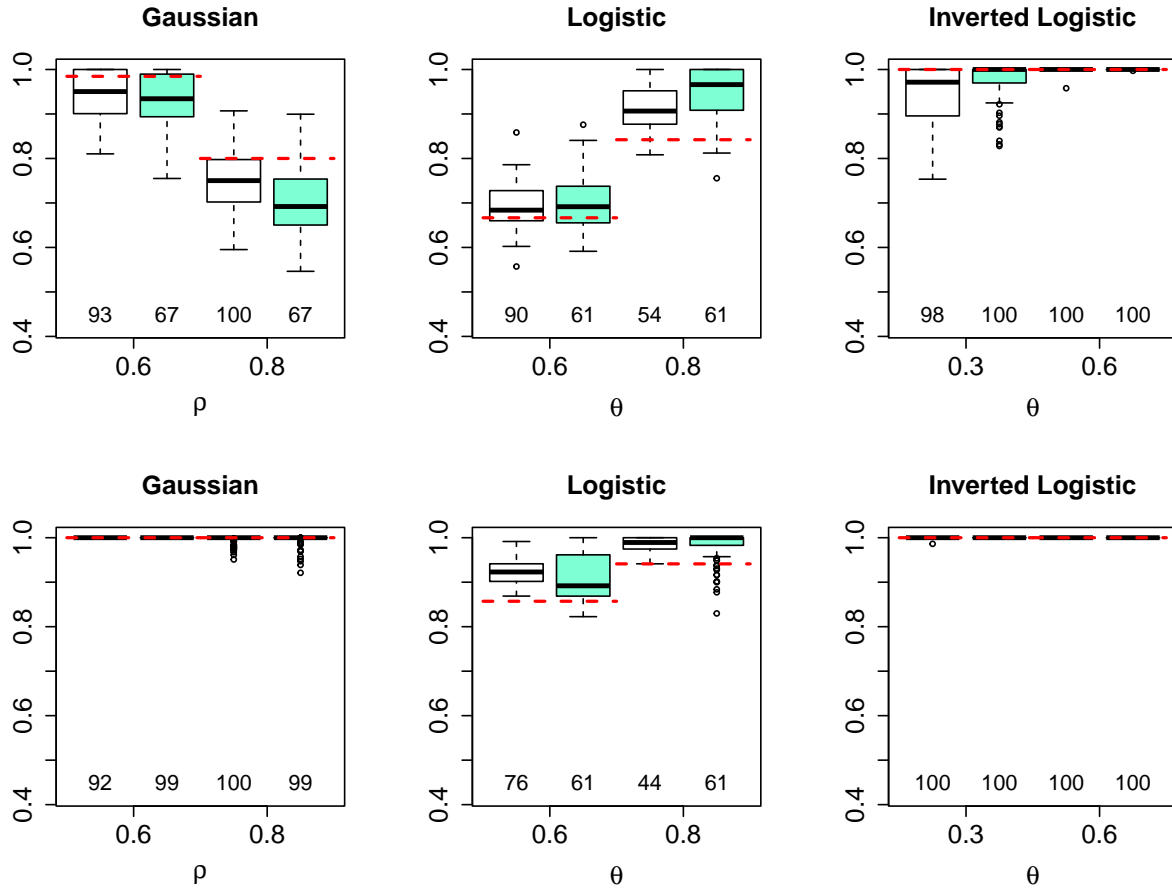


Figure 8: Sampling distribution of the posterior medians of $\tau_1(0.25)$ (top) and $\tau_1(0.75)$ (bottom) based on the Bézier spline estimator (white) for the three dependence copulas, alongside estimates using the Simpson-Tawn estimator (green). The red lines indicate the true values, and coverage of equi-tailed 95% intervals are noted below each boxplot.

Table 3: Average posterior probability of asymptotic dependence ($\eta = 1$) over simulated datasets for the three copulas.

Setting	Gaussian		Logistic		Inverted Logistic	
	$\rho = 0.6$	$\rho = 0.8$	$\theta = 0.6$	$\theta = 0.8$	$\theta = 0.3$	$\theta = 0.6$
$\Pr(\eta = 1 \mathbf{X})$	0.03	0.26	0.87	0.67	0.03	0.00

outperforms the Bézier spline estimator in over half the half the dependence measures considered. This is likely due to the relatively low prior probability placed on point masses at 0 for this copula, leading to higher errors especially in low dependence cases.

Table 3 summarizes the posterior probability of $\eta = 1$ for the three cases, averaged over the 100 datasets. The probability is higher than 0.5 only for the logistic case, where the underlying process has asymptotic dependence. In the other two cases, higher posterior probabilities of $\eta = 1$ appear as dependence gets stronger, but are very low overall. We conclude that the Bézier splines are adept at representing limit set boundaries associated with common parametric copula models, and are also flexible enough to represent a wider variety of edge cases. In all cases, the true value of η was well-estimated from the posterior distribution, and the model is particularly adept at identifying asymptotic dependence.

4.2 Comparison of truncated and censored Gamma likelihoods

4.2.1 Study setup

For each copula and parameter combination, we generate 100 datasets of $n = 600$ data points each, which we then convert to pseudo-polar coordinates. For the truncated Gamma approach, the gauge functions are estimated based on just the points that are above the quantile threshold level for at least one of the variables; we consider $\tau = 0.80$ and $\tau = 0.90$ to explore the behavior of the estimator under data scarcity. For the censored Gamma approach, the gauge functions are estimated based on all 600 points, with the likelihood censored below $\tau = 0.95$. The remainder of the study is set up identically to the previous section.

4.2.2 Parameter estimates

Figure 9 shows boxplots of the posterior median of η for the three dependence copulas. The blue boxplots correspond to estimates based on the truncated Gamma likelihood, while the white boxplots correspond to estimates based on a censored Gamma likelihood. For the truncated estimator, the top row plots estimates of η for $\tau = 0.80$ and the bottom row plots estimates for $\tau = 0.90$. Analytical values of η are shown as red lines on each plot. The coverage of equi-tailed 95% intervals are noted in plain text below each boxplot. Both estimators have nominal coverage, and the estimated η for the truncated estimator increases with the threshold level. While this means that the truncated estimator overestimates η in most cases compared to the censored estimator, it is a better estimator for the logistic copula. However, the censored estimator has lower bias in all remaining study settings. Additionally, we found that the censored estimator is not particularly sensitive to the threshold level for values higher than $\tau = 0.90$, whereas the truncated estimator provides higher and higher estimates of η as less and less data is available beyond the threshold level.

As in the previous study, we calculate the RMSE for η and the RMISE for $\lambda(\omega)$ and $\tau_1(\delta)$ based on posterior medians, for $\omega, \delta = 0.01, 0.02, \dots, 0.99$. For the truncated Gamma case, we focus on the $\tau = 0.80$ setting. Table 4 contains RMSE ratios for η based on the two estimators, as well as RMISE ratios for $\lambda(\omega)$ and $\tau_1(\delta)$. The ratio calculates the relative performance of using truncated Gamma and censored Gamma likelihoods to estimate the gauge functions; values greater than 1 indicate that the censored estimator has lower RMSE than the truncated estimator. In two-thirds of the study configurations, the censored estimator has lower RMSE/RMISE compared to the truncated estimator. The exception, as mentioned previously, is for the logistic copula. In this case, both estimators underestimate η , but the truncated estimator has lower bias compared to the censored estimator. While the truncated estimator is marginally better at identifying asymptotic dependence in the data in this study, the censored estimator has overall lower bias and RMSE/RMISE in most scenarios.

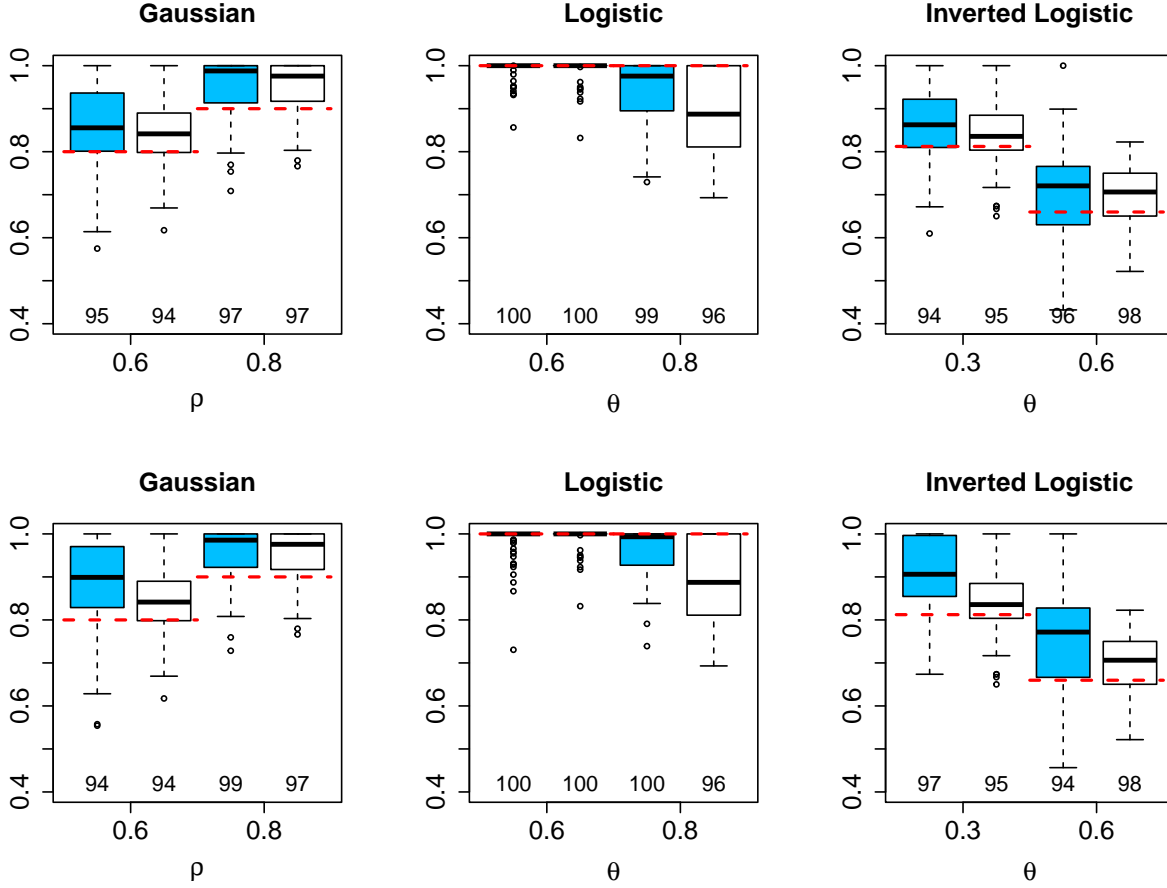


Figure 9: Sampling distribution of the posterior medians of η based on the Bézier splines for the three dependence copulas using truncated (blue) and a censored (white) Gamma likelihood. For the truncated Gamma likelihood model, the top and bottom rows considers thresholds of $\tau = 0.80$ and $\tau = 0.90$ respectively. The censored Gamma likelihood model is evaluated at a threshold of $\tau = 0.95$ in both cases. The red lines indicate the true values, and coverage of equi-tailed 95% intervals are noted below each boxplot.

Table 4: RMSE ratios for estimates of η and RMISE ratios for estimates of $\lambda(\omega)$ and $\tau_1(\delta)$ based on the Bézier splines with truncated Gamma (T) and censored Gamma (C) likelihoods, with quantile levels $\tau = 0.80$ and $\tau = 0.95$ respectively for the two cases.

	Gaussian		Logistic		Inverted logistic	
	$\rho = 0.6$	$\rho = 0.8$	$\theta = 0.6$	$\theta = 0.8$	$\theta = 0.3$	$\theta = 0.6$
$\frac{RMSE(\hat{\eta}_T)}{RMSE(\hat{\eta}_C)}$	1.29	1.07	0.95	0.70	1.24	1.42
$\frac{RMISE(\hat{\lambda}_T)}{RMISE(\hat{\lambda}_C)}$	1.33	1.23	0.80	0.65	1.13	1.33
$\frac{RMISE(\hat{\tau}_T)}{RMISE(\hat{\tau}_C)}$	1.14	1.12	1.00	0.93	1.11	1.29

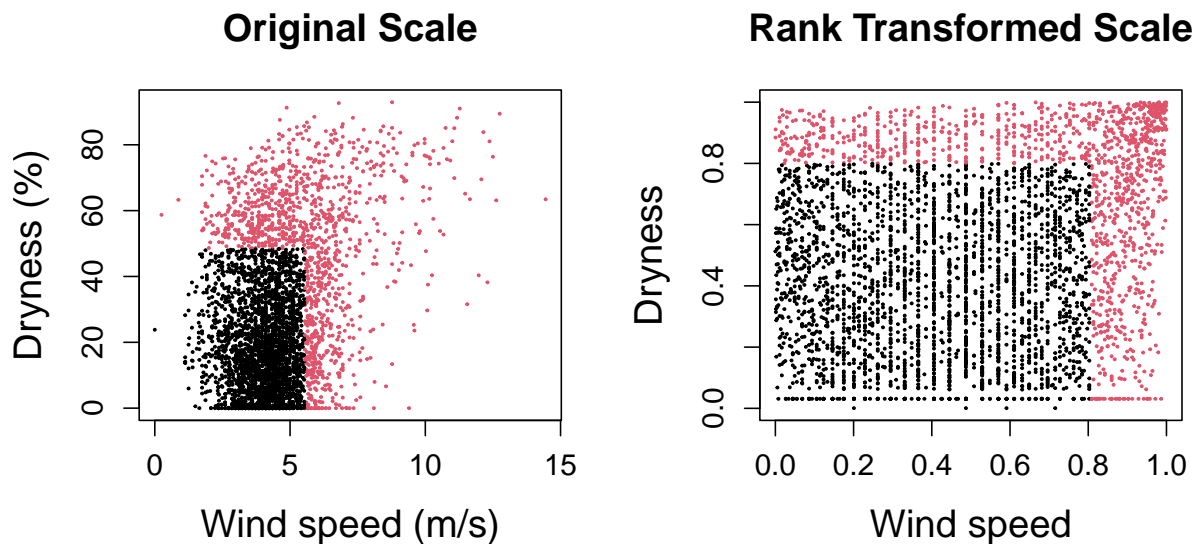


Figure 10: Santa Ana wind speeds and dryness measured at the March Air Force Base station. Data above 0.80 marginal quantile threshold are in red.

In summary, choosing between the two approaches largely comes down to data availability. In our testing, if a few thousand data points are available, the truncated and censored Gamma approaches provides comparable estimates, but the computational costs for the censored Gamma approach is several times higher and makes it impractical and unnecessary. If the data is limited to fewer than one thousand observations, the censored Gamma model is a viable alternative to the truncated Gamma model due to its manageable computational cost and low sensitivity to the choice of quantile threshold.

5 Applications

We consider two applications for estimating gauge functions using Bézier splines. The first application considers the tail dependence between wind speed and dryness at the March Air Force Base station in California. Both variables are indicators of fire weather, and high estimates of η would indicate that they affect extreme fire weather simultaneously. The second application concerns the tail dependence between observed and modeled ozone data at 519 station locations across the US. In this case, we want to verify whether the numerical model data is consistent with observational data at higher quantiles. In both cases, we apply rank transformations to the data which put them on the uniform scale marginally. We are then able to transform the data to exponential margins and estimate the gauge function for data points above high quantile thresholds.

5.1 Analysis of the Santa Ana Winds data

We apply our method to the Santa Ana winds and dryness data (Cooley et al., 2019). The Santa Ana winds are a multivariate meteorological regime that has been implicated as a major driver of large wildfires in southern California (Billmire et al., 2014). Wildfires are related to several conditions like temperature, humidity, wind speed, and fuel supply (Littell et al., 2018). Historically, the autumn months of September, October, and November have had a higher number of wildfires compared to the winter months, and are associated with warm temperatures, low humidity, and high winds. Cooley et al. (2019) surmised that the data exhibits asymptotic dependence, and used a modeling framework where all asymptotic independence is a degenerate case corresponding to exact dependence.

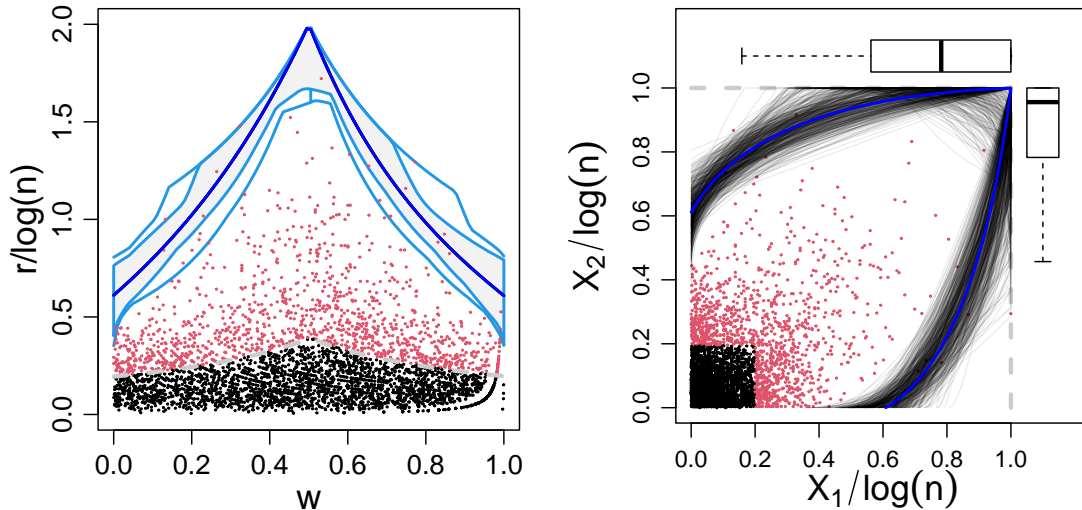


Figure 11: Limit set boundaries based on Bézier splines in pseudo-polar space (left) and Euclidean space (right) for assessing tail dependence between Santa Ana windspeed and relative humidity. Median curves are plotted in dark blue.

We consider daily dryness (%) and wind speed (m/s) data collected at the March Air Reserve Base station in Riverside County from the HadISD dataset (Dunn et al., 2012). The dryness is defined in this case as the $100 - \text{RH}$, where RH is the relative humidity measured as a percentage. The bivariate time series represents a measure of the daily risk of fire. The station’s variables have appeared to be associated with known Santa Ana events. The data consists of 3,902 days for the months of September–November from 1972–2015; we assume temporal stationarity as in Cooley et al. (2019). Figure 10 plots the data both in its original scale as well as the rank transformed scale. The data shows tail dependence, noticeable in the rank transformed data with a cluster of values in the upper right corner. Our goal is to study the tail dependence between the two variables by estimating a gauge function for the data after a further transformation to unit exponential margins.

We analyze this data at a threshold of $\tau = 0.80$, providing us with 1,234 points that are above the threshold in at least one margin. The conditional distribution of the radii are assumed to be a truncated Gamma distribution for this analysis. We run 2 MCMC chains of 15,000 iterations each, discarding the first 5,000 from each chain as burn-in. The priors and the remainder of the MCMC settings are identical to the simulation study.

Figure 11 plots the estimated limit set boundaries, with the median curve plotted in blue. The plot on the left is in pseudo-polar coordinates and depicts an functional boxplot of the estimated limit set boundary, while the plot on the right is in Euclidean coordinates. The posterior median of η is estimated to be 1, and $\Pr(\eta = 1 | \mathbf{X}) = 0.61$, suggesting asymptotic dependence between wind speed and dryness. To test sensitivity to the threshold level and to the prior probability of p_2, p_3 , or p_4 having a point mass at 1 (which would result in asymptotic dependence), we repeated the experiment at an additional threshold level $\tau = 0.90$ and the prior probability of a point mass at (1,1) as 0.01 (instead of the default setting of 0.025). This gives us a total of 3 additional study settings. In all 3 cases, $\Pr(\eta = 1 | \mathbf{X}) > 0.40$ and the third quantile of the posterior of η is 1, with the median being 1 when the prior probability of a point mass is unchanged. Taken together, we conclude that dryness and windspeed for the Santa Ana dataset is asymptotically dependent with high probability, consistent with the results of Cooley et al. (2019).

5.2 Analysis of Ozone concentration data

For our second study, we consider air pollution measurement data across the US from the Community Multiscale Air Quality (CMAQ) model (Binkowski and Roselle, 2003; Wyatt Appel et al., 2007, 2008) as well

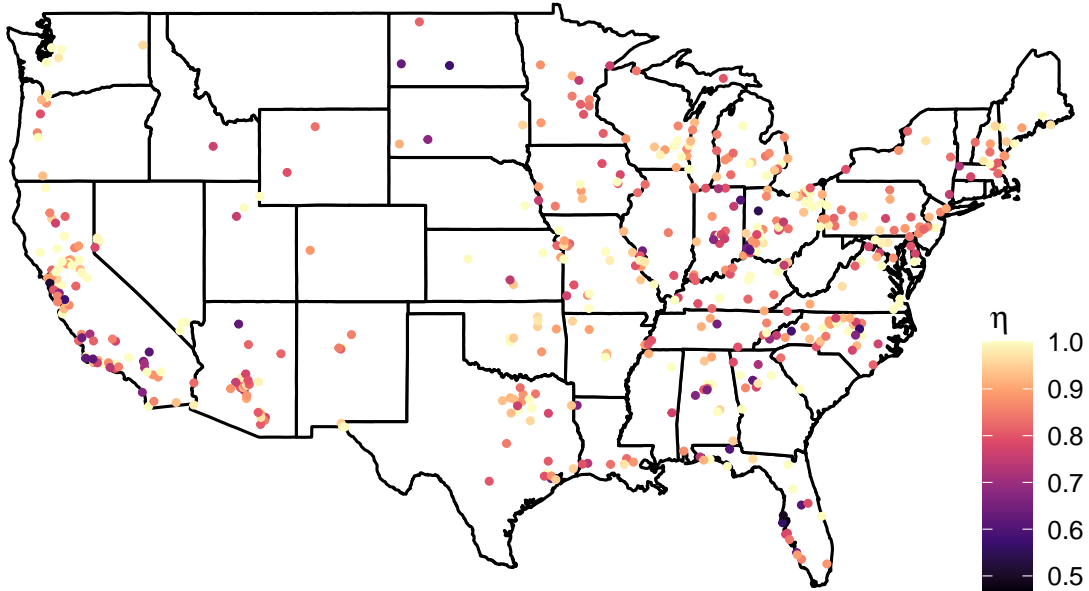


Figure 12: Posterior median of η at 519 AQS monitoring stations in the US.

as EPA Air Quality System (AQS) (US EPA, 2017) data for the contiguous US. While CMAQ is a numerical model available across the entire country at a 12km resolution, the AQS dataset consists of observations monitored at 1,376 stations across the US. Among them, only 519 stations had over 600 observations, which is what we use for this analysis. The full dataset has previously been used by Gong et al. (2021) to develop a combined data product for 12 air pollutants. When fusing data products, it is important to calibrate the model data to ground truth. In our application, we will verify how strong the dependence is between the AQS and CMAQ datasets for ozone, one of the 12 pollutants made available by both datasets.

Our data consists of daily ozone readings for the months of July–September from 2010–2014, resulting in a bivariate time series of CMAQ and AQS data for up to 610 days at each station. The sample correlations between the AQS and CMAQ data for the 519 stations range from 0.29–0.86 with a median of 0.69, suggesting a high level of agreement in the bulk of the distribution. To assess tail dependence, we fit a gauge function with censored Gamma likelihood for data censored at $\tau = 0.95$ threshold independently at every station. We run 2 MCMC chains for 11,000 iterations each for each station’s data, discarding the first 1,000 as burn-in.

The posterior median of η has an average value of 0.87 across the 519 locations, and is 1 (asymptotically dependent) for 108 of those stations. When repeated with a truncated Gamma likelihood estimator with a threshold of $\tau = 0.90$, we obtained an average η of 0.89 with asymptotic dependence at 159 locations. This suggests that the CMAQ data product can adequately represent the tail behavior of observational ambient ozone. Finally, Figure 12 plots the posterior probability of asymptotic dependence based on the censored Gamma model. While we are unable to discern any spatial pattern for high or low posterior values of η from the map, we do note that several of the low values are in urban areas with high population densities.

6 Discussion

Key aspects of tail dependence in multivariate distributions can be described through their corresponding gauge functions. In this study, we propose a semi-parametric method for estimating gauge functions by modeling their unit level sets as Bézier splines comprised of three quadratic Bézier curves. The splines can represent the gauge function unit level sets, and hence limit set boundaries, of varying shapes, and are parsimoniously parameterized by a small number of control points. The quadratic specification makes it straightforward to obtain analytical solutions for the shape of the limit set, and constraints on the control points ensure that the resultant shapes are valid limit set boundaries. Bayesian estimation of the Bézier splines requires only standard MCMC techniques and allows important cases on the edge of the parameter space to be represented by employing mixture priors with point masses. We demonstrate the efficacy of our model using numerical studies as well as two real data applications involving fire weather in California, and ambient air pollution from ozone across the US.

We have only considered bivariate random vectors here, but the modeling strategy scales relatively straightforwardly to three dimensions by using Bézier surfaces and requiring more complicated constraints. Dimensions greater than three appear to be infeasible.

In addition, it appears possible to extend our modeling framework to include negative dependence by transforming to Laplace margins rather than exponential margins. This has been previously suggested (Simpson and Tawn, 2022; Wadsworth and Campbell, 2022) and recently implemented in the context of radially stable Pareto distributions (Papastathopoulos et al., 2023). Implementing our Bézier model in Laplace margins would probably require adding a small number of additional control points and specifying appropriate constraints on their support.

Funding

This work was supported by grants from the Southeast National Synthesis Wildfire and the United States Geological Survey’s National Climate Adaptation Science Center (G21AC10045), and the National Science Foundation (DMS-2001433, DMS-2152887).

References

- Balkema, A. A., Embrechts, P., and Nolde, N. (2010), “Meta densities and the shape of their sample clouds,” *J. Multivariate Anal.*, 101, 1738–1754.
- Balkema, G. and Nolde, N. (2010), “Asymptotic independence for unimodal densities,” *Adv. in Appl. Probab.*, 42, 411–432.
- Billmire, M., French, N. H. F., Loboda, T., Owen, R. C., and Tyner, M. (2014), “Santa Ana winds and predictors of wildfire progression in southern California,” *Int. J. Wildland Fire*, 23, 1119–1129.
- Binkowski, F. S. and Roselle, S. J. (2003), “Models-3 Community Multiscale Air Quality (CMAQ) model aerosol component 1. Model description,” *J. Geophys. Res. - Atmos.*, 108.
- Cooley, D., Hunter, B. D., and Smith, R. L. (2019), “Univariate and multivariate extremes for the environmental sciences,” in *Handbook of environmental and ecological statistics*, Chapman and Hall/CRC, pp. 153–180.
- Davis, R. A., Mulrow, E., and Resnick, S. I. (1988), “Almost sure limit sets of random samples in \mathbf{R}^d ,” *Adv. in Appl. Probab.*, 20, 573–599.
- Dunn, R. J. H., Willett, K. M., Thorne, P. W., Woolley, E. V., Durre, I., Dai, A., Parker, D. E., and Vose, R. S. (2012), “HadISD: a quality-controlled global synoptic report database for selected variables at long-term stations from 1973–2011,” *Clim. Past*, 8, 1649–1679.
- Farouki, R. T. (2012), “The Bernstein polynomial basis: a centennial retrospective,” *Comput. Aided Geom. D.*, 29, 379–419.

- Gong, W., Reich, B. J., and Chang, H. H. (2021), “Multivariate spatial prediction of air pollutant concentrations with INLA,” *Environ. Res. Commun.*, 3, 101002.
- Hazewinkel, M. (2012), *Encyclopaedia of Mathematics*, no. Vol. 1 in Encyclopaedia of Mathematics, Springer Netherlands.
- Heffernan, J. E. and Tawn, J. A. (2004), “A conditional approach for multivariate extreme values,” *J. R. Stat. Soc. Ser. B Stat. Methodol.*, 66, 497–546, with discussions and reply by the authors.
- Hill, B. M. (1975), “A Simple General Approach to Inference About the Tail of a Distribution,” *Ann. Stat.*, 3, 1163–1174.
- Hyndman, R. J. and Shang, H. L. (2010), “Rainbow Plots, Bagplots, and Boxplots for Functional Data,” *J. Computat. Graph. Stat.*, 19, 29–45.
- Kinoshita, K. and Resnick, S. I. (1991), “Convergence of scaled random samples in \mathbf{R}^d ,” *Ann. Probab.*, 19, 1640–1663.
- Ledford, A. W. and Tawn, J. A. (1996), “Statistics for near independence in multivariate extreme values,” *Biometrika*, 83, 169–187.
- Littell, J. S., McKenzie, D., Wan, H. Y., and Cushman, S. A. (2018), “Climate Change and Future Wildfire in the Western United States: An Ecological Approach to Nonstationarity,” *Earth’s Future*, 6, 1097–1111.
- López-Pintado, S. and Romo, J. (2009), “On the Concept of Depth for Functional Data,” *J. Am. Stat. Assoc.*, 104, 718–734.
- Majumder, R., Reich, B. J., Shaby, B. A., and Cooley, D. S. (2023), “Supplement to “Semiparametric Estimation of the Shape of the Limiting Multivariate Point Cloud”,” .
- Marcon, G., Padoan, S., Naveau, P., Muliere, P., and Segers, J. (2017), “Multivariate nonparametric estimation of the Pickands dependence function using Bernstein polynomials,” *J. Stat. Plan. Infer.*, 183, 1–17.
- Marcon, G., Padoan, S. A., Naveau, P., and Muliere, P. (2014), “Nonparametric estimation of the dependence among multivariate rainfall maxima,” in *METMA VII-GRASPA 14*.
- Murphy-Barltrop, C., Wadsworth, J., and Eastoe, E. (2023), “Improving estimation for asymptotically independent bivariate extremes via global estimators for the angular dependence function,” *arXiv preprint*, arXiv:2303.13237.
- Nolde, N. (2014), “Geometric interpretation of the residual dependence coefficient,” *J. Multivariate Anal.*, 123, 85–95.
- Nolde, N. and Wadsworth, J. L. (2022), “Linking representations for multivariate extremes via a limit set,” *Adv. Appl. Probab.*, 54, 688–717.
- Papastathopoulos, I., De Monte, L., Campbell, R., and Rue, H. (2023), “Statistical inference for radially-stable generalized Pareto distributions and return level-sets in geometric extremes,” *arXiv preprint*, arXiv:2310.06130.
- Simpson, E. S. and Tawn, J. A. (2022), “Estimating the limiting shape of bivariate scaled sample clouds for self-consistent inference of extremal dependence properties,” *arXiv preprint*, arXiv:2207.02626.
- Simpson, E. S., Wadsworth, J. L., and Tawn, J. A. (2020), “Determining the dependence structure of multivariate extremes,” *Biometrika*, 107, 513–532.
- Sun, Y. and Genton, M. G. (2011), “Functional Boxplots,” *J. Computat. Graph. Stat.*, 20, 316–334.
- US EPA (2017), “Air Quality System Database,” Accessed on 3 August, 2017.

- Vettori, S., Huser, R., and Genton, M. G. (2018), “A comparison of dependence function estimators in multivariate extremes,” *Stat. Comput.*, 28, 525–538.
- Wadsworth, J. L. and Campbell, R. (2022), “Statistical inference for multivariate extremes via a geometric approach,” *arXiv preprint*, arXiv:2208.14951v1.
- Wadsworth, J. L. and Tawn, J. A. (2013), “A new representation for multivariate tail probabilities,” *Bernoulli*, 19, 2689–2714.
- Wyat Appel, K., Bhave, P. V., Gilliland, A. B., Sarwar, G., and Roselle, S. J. (2008), “Evaluation of the community multiscale air quality (CMAQ) model version 4.5: Sensitivities impacting model performance; Part II—particulate matter,” *Atmos. Environ.*, 42, 6057–6066.
- Wyat Appel, K., Gilliland, A. B., Sarwar, G., and Gilliam, R. C. (2007), “Evaluation of the Community Multiscale Air Quality (CMAQ) model version 4.5: Sensitivities impacting model performance: Part I—Ozone,” *Atmos. Environ.*, 41, 9603–9615.

Supplementary Material for ‘Semiparametric Estimation of the Shape of the Limiting Multivariate Point Cloud’

Reetam Majumder, Benjamin A. Shaby, Brian J. Reich, and Daniel S. Cooley

A Comparison of Threshold Selection Approaches

A.1 Connection to the main text

This simulation study supports Section 3.1 of the main text, and investigates the sensitivity of the form of threshold used to select data from the joint tail on the estimation of η .

A.2 Different forms of the threshold

Previous works (??) have used elaborate schemes to specify a good threshold as part of their pipelines for estimating the gauge function. These schemes all in essence come down to some version of estimating a conditional high quantile of radii, as a function of angle. However, both the truncated and censored gamma likelihoods that we use here contain terms that account for the magnitude of the threshold at any given angle, so it is not obvious to us why choosing a complicated threshold is necessary for estimating the gauge function. To explore this issue, we compare three schemes for choosing the threshold, which range from the simplest available choice to the unattainably ideal.

The first scheme is the *marginal threshold*, which sets a threshold in each margin, independently, at a fixed marginal empirical quantile τ . The second scheme, which we call the *radial threshold*, is a slight modification of the marginal threshold. The radial threshold enforces the threshold to be the same in both margins, and sets it so that a $1 - \tau$ proportion of points are above the threshold in at least one component. If the two marginal empirical *CDFs* are identical, then the marginal and radial thresholds coincide, but for differing quantile levels τ .

The final threshold is the *oracle threshold*. This threshold is based on the observation that the conditional quantile is inversely proportional to the gauge function, evaluated at any angle, at high quantiles (?). That is,

$$q_\tau(w) \approx \frac{C}{g(w)},$$

for some constant C , for large τ . In the context of a simulation, we know the gauge function $g(w)$ of the data-generating model, so for any simulated dataset we can choose C_0 such that the proportion of radii that exceed $\frac{C_0}{g(w)}$ is $1 - \tau$. We then set the threshold $r_0(w) = \frac{C_0}{g(w)}$. This threshold is therefore an asymptotic approximation to the true conditional quantile $q_\tau(w)$. We call it the oracle threshold because it requires knowledge of the true gauge function $g(w)$, which is of course unavailable outside of simulations. One can think of it as an unrealistically good conditional quantile estimate.

To put all of the thresholds on even footing for the purposes of gauge function estimation, we force them to include the same number of points available for estimation. Let the 2 variables under consideration be X_1 and X_2 ; we denote their marginal quantiles as q_1 and q_2 , where the quantiles are selected at the $\tau = 0.80$ level. Further, let n denote the number of observations in our study. The *marginal threshold* that we use in our study selects (X_1, X_2) points for which either $X_1 > q_1$, or $X_2 > q_2$, or both. The number of points that are selected above the threshold using this approach is of course higher than $n(1 - \tau)$; this is denoted n_0 in Eqn. (2) of the main text. We then adjust the nominal quantile level τ when calculating the radial and oracle thresholds, such that each results in n_{marg} points available for model fitting.

Table A.1: Average posterior probability of asymptotic dependence ($\eta = 1$) over simulated datasets for the three copulas, with data selected using three different thresholding methods.

Threshold	Gaussian		Logistic		Inverted Logistic	
	$\rho = 0.6$	$\rho = 0.8$	$\theta = 0.6$	$\theta = 0.8$	$\theta = 0.3$	$\theta = 0.6$
Marginal	0.028	0.255	0.87	0.67	0.033	0.000
Radial	0.029	0.259	0.87	0.68	0.034	0.000
Oracle	0.010	0.107	0.86	0.55	0.019	0.000

A.3 Results

For each of the 6 combinations of copulas and dependence levels, we generate 100 datasets of $n = 5,000$ data points. The analysis based on the marginal threshold is identical to the simulation study presented in Section 4.1 of the main text, at the quantile level of $\tau = 0.80$. We also extract the number of points used for fitting the truncated Gamma likelihood for the 100 datasets. This number is different for each of the 100 datasets, and we denote them $n_0^{(1)}, \dots, n_0^{(100)}$. To evaluate model fit based on the radial and oracle thresholds, we select $n_0^{(1)}, \dots, n_0^{(100)}$ points respectively from the 100 datasets based on each thresholding approach. This ensures that the truncated Gamma likelihood is fitted to the same number of points in each case. The MCMC simulations are carried out using the same settings as the simulation study in Section 4.1.

Table A.1 summarizes the posterior probability of $\eta = 1$ for each case, averaged over the 100 datasets. Results based on the marginal and radial thresholds are very similar to each other in all cases. The oracle threshold provides the best estimates of the posterior probability all cases except for the logistic copula with low dependence ($\theta = 0.8$), where it is worse than both the marginal and radial approaches.

Figure A.1 shows boxplots of the posterior median of η for the different cases. Analytical values of η are shown as red lines in each plot, and the coverage of equi-tailed 95% intervals are noted below each boxplot. Results from the radial and marginal threshold approaches are both competitive with the oracle threshold results in every case. In particular, when the posterior dependence is low (middle-right and bottom-right plots), the marginal and radial thresholds have less bias and better coverage than the oracle threshold. This indicates that the very simple marginal threshold performs comparably to the (unattainable) oracle threshold. We thus proceed by eschewing complicated threshold calculation requiring quantile regression, and simply use the marginal threshold.

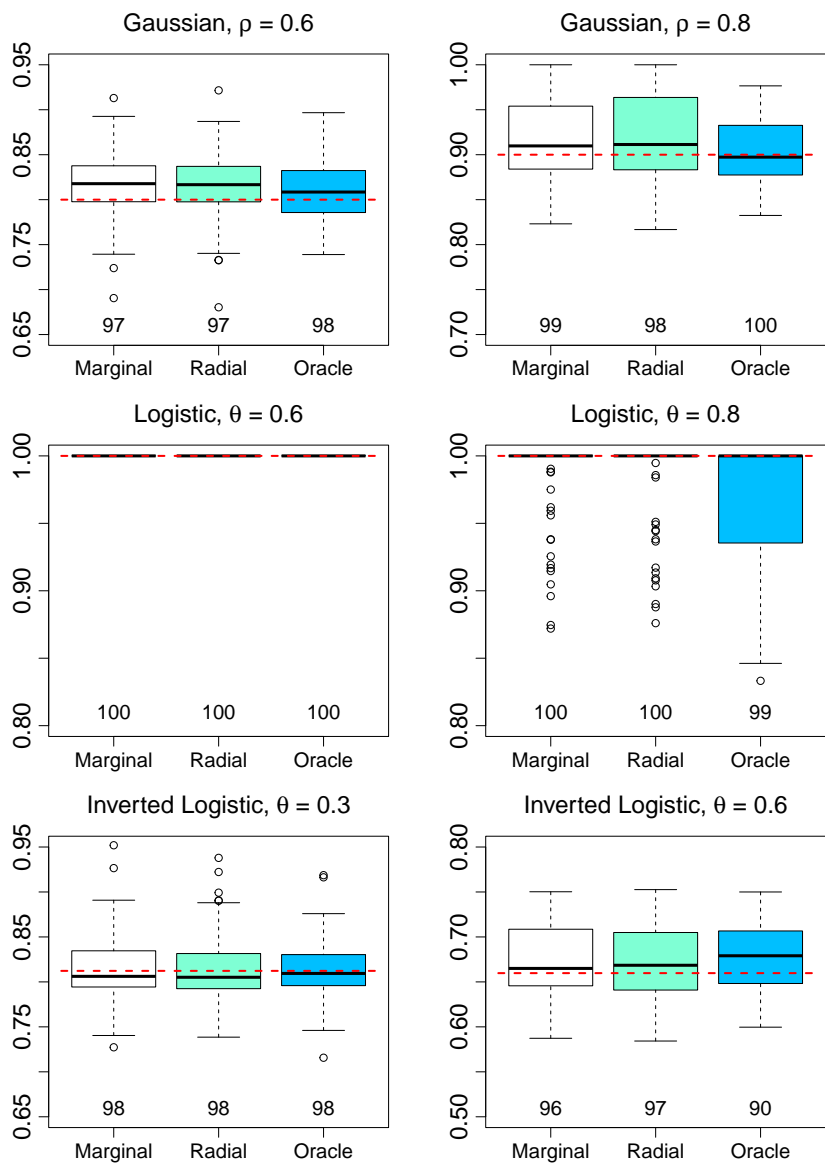


Figure A.1: Sampling distribution of the posterior medians of η based on Bézier spline estimates of tail behavior, with data selected using three different thresholding methods. The red lines indicate the true values, and coverage of equi-tailed 95% intervals are noted below each plot.

B Comparison of the Different Estimators

B.1 Connection to the main text

This Appendix supports Section 4 of the main text, and provides the RMSE/RMISE estimates of η , $\lambda(\omega)$, and $\tau_1(\delta)$ based on the different forms of the Bézier spline estimator under consideration.

B.2 Results

Table B.1 contains the raw RMSE/RMISE values used to generate the ratios that are provided in Table 2 of the main text, comparing the Bézier spline and Simpson-Tawn estimators. Table B.2 contains the raw RMSE/RMISE values used to generate the ratios that are provided in Table 4 of the main text, comparing the truncated Gamma and censored Gamma likelihoods for modeling tail behavior.

Table B.1: RMSE for estimates of η and RMISE for estimates of $\lambda(\omega)$ and $\tau_1(\delta)$ based on the Bézier spline ($\hat{\eta}$, $\hat{\lambda}$, and $\hat{\tau}$) and Simpson-Tawn ($\tilde{\eta}$, $\tilde{\lambda}$, and $\tilde{\tau}$) estimators over simulated datasets for the three copulas.

	Gaussian		Logistic		Inverted logistic	
	$\rho = 0.6$	$\rho = 0.8$	$\theta = 0.6$	$\theta = 0.8$	$\theta = 0.3$	$\theta = 0.6$
$\hat{\eta}$	0.039	0.054	0.000	0.030	0.039	0.048
$\tilde{\eta}$	0.048	0.055	0.021	0.082	0.040	0.034
$\hat{\lambda}$	0.014	0.008	0.000	0.004	0.014	0.035
$\tilde{\lambda}$	0.019	0.009	0.002	0.031	0.016	0.031
$\hat{\tau}_1$	0.060	0.060	0.061	0.072	0.114	0.028
$\tilde{\tau}_1$	0.061	0.085	0.068	0.093	0.020	0.003

Table B.2: RMSE for estimates of η and RMISE for estimates of $\lambda(\omega)$ and $\tau_1(\delta)$ based on the Bézier splines with truncated Gamma (T) and censored Gamma (C) likelihoods, with quantile levels $\tau = 0.80$ and $\tau = 0.95$ respectively for the two cases.

	Gaussian		Logistic		Inverted logistic	
	$\rho = 0.6$	$\rho = 0.8$	$\theta = 0.6$	$\theta = 0.8$	$\theta = 0.3$	$\theta = 0.6$
$\hat{\eta}_C$	0.090	0.079	0.023	0.144	0.081	0.077
$\hat{\eta}_T$	0.115	0.085	0.022	0.101	0.100	0.109
$\hat{\lambda}_C$	0.026	0.012	0.003	0.032	0.025	0.055
$\hat{\lambda}_T$	0.035	0.015	0.003	0.021	0.029	0.072
$\hat{\tau}_{1C}$	0.086	0.072	0.103	0.083	0.144	0.059
$\hat{\tau}_{1T}$	0.098	0.080	0.104	0.078	0.159	0.077